K^- multi-nucleon absorption cross sections and branching ratios in Λp and $\Sigma^0 p$ final states

R. Del Grande[a], K. Piscicchia[b,a], O. Vazquez Doce[c,d], M. Cargnelli[e], C. Curceanu[a], L. Fabbietti[c,d], J. Marton[e], P. Moskal[f], A. Ramos[g], A. Scordo[a], D. Sirghi[a], M. Skurzok[f], S. Wycech[h], J. Zmeskal[e], E. Czerwinski[f], V. De Leo[i], P. Fermani[a], G. Mandaglio[j,k], M. Martini[a,l], N. Raha[i], A. Selce[m,n], M. Silarski[f]

[a] *INFN - Laboratori Nazionali di Frascati, Via Enrico Fermi 40, 00044, Frascati, Italy*
[b] *CENTRO FERMI - Museo Storico della Fisica e Centro Studi e Ricerche "Enrico Fermi", 00184, Rome, Italy*
[c] *Excellence Cluster "Origin and Structure of the Universe", 85748 Garching, Germany*
[d] *Physik Department E12, Technische Universität München, 85748 Garching, Germany*
[e] *Stefan-Meyer-Institut für Subatomare Physik, 1090 Wien, Austria*
[f] *Institute of Physics, Jagiellonian University, 30-348 Cracow, Poland*
[g] *Departament de Fisica Quantica i Astrofisica and Institut de Ciencies del Cosmos, Universitat de Barcelona, Marti i Franques 1, 08028 Barcelona, Spain*
[h] *National Centre for Nuclear Research, 00681 Warsaw, Poland*
[i] *INFN Sezione di Roma Tor Vergata, Roma, Italy*
[j] *Dipartimento di Scienze Chimiche, Biologiche, Farmaceutiche ed Ambientali dell'Università di Messina, Messina, Italy*
[k] *INFN Sezione di Catania, Catania, Italy*
[l] *Dipartimento di Scienze e Tecnologie applicate, Università "Guglielmo Marconi", Roma, Italy*
[m] *Dipartimento di Matematica e Fisica dell'Università "Roma Tre", Roma, Italy*
[n] *INFN Sezione di Roma Tre, Roma, Italy*

Abstract

The determination of low-energy cross sections and branching ratios of the K^- multi-nucleon absorption processes in Λp and $\Sigma^0 p$ final states performed by the AMADEUS collaboration is presented. Low momentum K^- ($p_K \simeq 127$ MeV/c) produced at the DAΦNE collider are impinged on a Carbon target within the KLOE detector and the two and three nucleon

Email addresses: raffaele.delgrande@lnf.infn.it (R. Del Grande), kristian.piscicchia@gmail.com (K. Piscicchia), oton.vd@cern.ch (O. Vazquez Doce)

absorption processes are disentangled by comparing the experimental data to phenomenological calculations. The Λp spectra are entirely interpreted in terms of K^- multi-nucleon absorption processes; the possible contribution of a K^-pp bound state is demonstrated to overlap with the two nucleon capture process, its absolute yield thus resulting indistinguishable.

Key words: strong interaction, strangeness nuclear physics, antikaon-nucleon interaction

1. Introduction

The investigation of the low-energy $\bar{K}N$ interaction is fundamental to quantitatively study the non-perturbative QCD in the strangeness sector. Furthermore, a quantitative understanding of the $\bar{K}N$ interaction could set solid constraints to the behaviour of the latter in dense nuclear medium and, hence, help in computing the equation of state for cold dense nuclear matter [1, 2, 3].

Chiral perturbation theory as well known in the pion-nucleon case cannot be applied to the low-energy strangeness QCD sector due to the existence of broad resonances just below the $\bar{K}N$ threshold (i.e. the isospin I=0 Λ(1405) and the I=1 Σ(1385)). Phenomenological potential models predict a strongly attractive $\bar{K}N$ interaction in the sub-threshold region, describing the Λ(1405) as a $\bar{K}N$ bound state, which implies the existence of deeply bound kaonic nuclear states [4, 5, 6, 7, 8, 9]. On the other hand, in the context of the chiral unitary SU(3) dynamics, the Λ(1405) emerges as a superposition of two states (whose relative contributions are not yet known), leading to a weaker $\bar{K}N$ interaction and to less tightly bound kaonic nuclear states [10, 11, 12, 13, 14].

From the experimental point of view the $\bar{K}$ -nucleon interaction has been studied by means of scattering experiments [15, 16, 17, 18, 19, 20, 21, 22, 23, 24], kaonic atoms [25, 26, 27, 28], measurements of kaon-nuclei absorption [29, 30, 31, 32] and search for deeply bound kaonic state in the most fundamental K^-pp system [33, 34, 35, 36, 37, 38, 39, 40, 41, 42]. These results confirm the $\bar{K}N$ interaction to be attractive and, recently, an experiment with high energy K^- beam ($p_K = 1$ GeV/c) showed evidence for the existence of a kaonic bound state [42]. For low-energy K^- induced reactions, the K^- bound states search cannot disregard a complete characterisation of the K^- multi-nucleon absorption, since the final states overlap over a broad region of the phase space [35, 43, 44, 40].

Information about in-medium properties of antikaons can be obtained in heavy-ion and proton-nucleus collisions at incident energies near or below the free nucleon-nucleon threshold (2.5 GeV) [45, 46, 47, 48, 49, 50, 51, 52, 53, 54, 55, 56, 57, 58, 59]. The experimental data are interpreted through comparisons with theoretical calculations and, in this context, the exclusive measurement of low energy antikaons off light nuclei is fundamental to constrain the theoretical interpretation of heavy-ion collisions.

A comprehensive understanding of the K^- multi-nucleon capture processes is far from being achieved: bubble chamber experiments provided only global K^- multi-nucleon branching ratios (BR) [29, 30, 31, 32]; few BRs for the K^--two and -three nucleon absorptions (2NA and 3NA) have been extracted within modern spectroscopic experiments [40, 60] and only 3NA cross sections for K^- momenta of 1 GeV/c are reported in Ref. [41]. The small ($\sim$1%) 2NA BR on deuteron compared to heavier nuclei led Wilkinson [61] to suggest a strong nuclear correlation among alpha particle type objects at nuclear surfaces. The multi-nucleon captures involve high momentum transfer and are then ideal to test the NN (or 3N, 4N) functions at short distances. This idea should be tested again using new data and the better understanding of nuclear theories.

This study aims to perform the first comprehensive measurement of the K^- 2NA, 3NA and 4NA BRs and cross sections for low-momenta kaons in Λp and Σ^0p channels. The contribution of the possible K^-pp bound state formation is also critically investigated. The K^- multi-nucleon absorptions are investigated by exploiting the hadronic interactions of negative kaons absorbed in ^{12}C nuclei, the main component of the Drift Chamber (DC) wall of the KLOE detector [62] at the DAΦNE collider [63]. The correlated production of a Λ and a proton in the final state of $K^-{}^{12}$C capture is studied.

2. Experimental setup

DAΦNE [63] (Double Annular Φ-factory for Nice Experiments) is a double ring $e^+ e^-$ collider, designed to work at the centre of mass energy of the ϕ particle. The ϕ mesons decaying nearly at-rest produce charged kaons with BR($K^+ K^-$) = (48.9 $\pm$ 0.5)% at low momentum ($\sim$ 127 MeV/c), ideal either to study reactions of stopped kaons, or to explore the products of the low energy nuclear absorptions of K^-. The back-to-back topology of the emitted K^-K^+ pairs allows to tag the K^- through the detection of a K^+ in the opposite direction, if the K^- track is not identified.

The KLOE detector [62] is centred around the interaction point of DAΦNE. KLOE is characterised by a $\sim 4\pi$ geometry and an acceptance of $\sim 98\%$; it consists of a large cylindrical Drift Chamber (DC) [64] and a fine sampling lead-scintillating fibres calorimeter [65], all immersed in an axial magnetic field of 0.52 T provided by a superconducting solenoid. The DC has an inner radius of 0.25 m, an outer radius of 2 m and a length of 3.3 m. The DC entrance wall composition is 750 μm of Carbon fibre and 150 μm of Aluminium foil. The KLOE DC is filled with a mixture of Helium and Isobutane (90% in volume ^{4}He and 10% C_4H_{10}). The chamber is characterised by excellent position and momentum resolutions: tracks are reconstructed with a resolution in the transverse $R-\phi$ plane $\sigma_{R\phi} \sim 200\,\mu$m and a resolution along the z-axis $\sigma_z \sim 2\,$mm, while the transverse momentum resolution for low momentum tracks ($(50 < p < 300)$MeV/c) is $\frac{\sigma_{p_T}}{p_T} \sim 0.4\%$.

The KLOE calorimeter is composed of a cylindrical barrel and two endcaps, providing a solid angle coverage of 98%. The volume ratio (lead/fibres/glue = 42:48:10) is optimised for a high light yield and a high efficiency for photons in the range (20-300) MeV/c. The photon detection efficiency is 99% for energies larger than 80 MeV and it falls to 80% at 20 MeV due to the cutoff introduced by the readout threshold. The position of the clusters along the fibres can be obtained with a resolution $\sigma_{\parallel} \sim 1.4\,\mathrm{cm}/\sqrt{E(\mathrm{GeV})}$. The resolution in the orthogonal direction is $\sigma_{\perp} \sim 1.3\,$cm. The energy and time resolutions for photon clusters are given by $\frac{\sigma_E}{E_\gamma} = \frac{0.057}{\sqrt{E_\gamma(\mathrm{GeV})}}$ and $\sigma_t = \frac{57\,\mathrm{ps}}{\sqrt{E_\gamma(\mathrm{GeV})}} \oplus 100$ ps.

An integrated luminosity of 1.74 fb^{-1} collected by the KLOE collaboration in the 2004/2005 data campaign is analysed. The inner wall of the KLOE DC is used as target. Dedicated GEANT Monte Carlo (MC) simulations of the KLOE apparatus (GEANFI [66]) were performed to estimate the percentages of K^- absorptions in the materials of the DC entrance wall (the K^- absorption physics treated by the GEISHA package). Out of the total fraction of captured kaons, about 81% is absorbed in the Carbon fibre component and the residual 19% in the Aluminium foil. Motivated by the larger amount of K^- captures in the Carbon fibre component and due to the similarity of the kinematic distributions for K^- absorptions in ^{12}C and ^{27}Al, not distinguishable within the experimental resolution, a pure Carbon target was considered in the analysis.

The analysed data include both K^- captures at-rest and in-flight. In the first case the negatively charged kaon is slowed down in the materials of the detector and consequently absorbed in a highly excited atomic orbit, from

which it cascades down till it is absorbed by the nucleus through the strong interaction. In the latter case the kaon penetrates the electronic cloud and interacts with the nucleus with an average momentum of about 100 MeV/c.

3. Λp events selection

The starting point of the analysis of K^- absorption processes is the identification of a Λ(1116) hyperon through its decay into a proton and a negatively charged pion (BR = (63.9 ± 0.5) % [67]).

The proton and pion tracks are identified using the dE/dx information measured in the DC wires, together with the energy information provided by the calorimeter. For each pion and proton candidate a minimum track length of 30 cm is required. Additionally, the proton candidate must have a momentum higher than $p > 170$ MeV/c in order to minimise the pion contamination in the proton sample and to improve the purity of the particle identification. A common vertex is searched for all the $p\pi^-$ pairs. The reconstructed invariant mass $m_{p\pi^-}$ shows a mean value of (1115.753 ± 0.002) MeV/c^2 and a resolution of $\sigma = 0.5$ MeV/c^2. For the next analyses steps, the following cut is applied on the $p\pi^-$ invariant mass: $(1112 < m_{p\pi^-} < 1118)$ MeV/c^2.

After the Λ decay vertex selection, the K^- hadronic interaction vertex is reconstructed. Events with an additional proton track are selected by applying the same cuts as for the protons associated to the Λ decay. The vertex position is determined by backward extrapolating the Λ path and the proton track with a resolution of 0.12 cm. At the point of closest approach, a distance smaller than 5 cm is required. Particles momenta are corrected for energy loss.

The distribution of the Λp (hadronic) vertices along the radial direction ($\rho_{\Lambda p}$), orthogonal with respect to the DAΦNE beam pipe, is used to select the K^-s absorptions occurring in the DC wall. The geometrical cut $\rho_{\Lambda p} = (25.0 \pm 1.2)$ cm was chosen to minimise the contamination from interactions with the gas of the DC [68].

The goal of this analysis is to extract the branching ratios and the low-energy cross sections for the K^- absorptions on two, three and four nucleons (2NA, 3NA and 4NA respectively), which are non-pionic processes:

$$K^- \text{“NN”} \rightarrow YN \qquad (2NA)\ , \tag{1}$$

$$K^- \text{“NNN”} \rightarrow Y(NN) \qquad (3NA)\ , \tag{2}$$

$$K^- \text{“NNNN”} \rightarrow Y(NNN) \qquad (4NA)\ , \tag{3}$$

where “NN”, “NNN” and “NNNN” are bound nucleons in the target nucleus, Y is the hyperon, (NN) and (NNN) represent the final state nucleons which can be bound or unbound. The main background source is represented by the pionic K^- single nucleon absorption processes:

$$K^- \text{“N”} \rightarrow Y\pi \qquad (1NA)\ , \tag{4}$$

that lead always to the production of a hyperon and a pion in the final state and whose global BR in ^{12}C is found to be about 80 % in emulsion experiments [32].

In the sample of the reconstructed Λp events an additional π^- or π^+ correlated with the Λp pair at the hadronic vertex, representing the signature of the K^- absorption on a single nucleon, is found in 16.3% and 6.1% of the total events, respectively. The correlated protons are produced as a consequence of the final state interaction (FSI) processes with fragmentation of the residual nucleus. Such events contribute to the lower region of the Λp invariant mass distribution and are characterised by low-momenta protons, as can be seen in Fig. 1. Since these protons originate from the residual nucleus

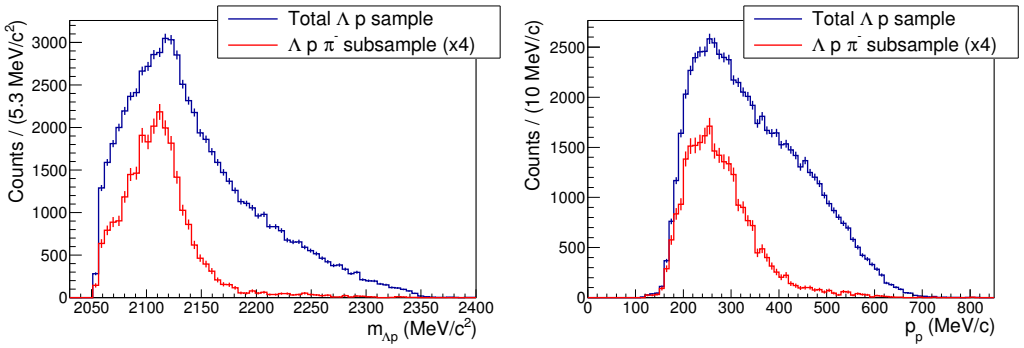

Figure 1: Λp invariant mass (left) and proton momentum (right) distributions are shown for the whole Λp data sample (blue) together with the Λpπ^- subsample events (red). The red distribution is multiplied by a factor 4 for a more clear comparison.

fragmentation, most of them are Fermi sea nucleons (the Fermi momentum distribution in ^{12}C is centred around 220 MeV/c), where the momentum distribution is partly distorted by the FSI processes.

As it will be shown at the end of this Section, the contribution of the K^- single nucleon absorptions to the selected Λp sample is strongly reduced

when the measurement of the mass of both selected protons (one from the Λ decay and the other from the FSI), by using the time of flight (TOF) information, is required, allowing to isolate an almost pure sample of multi-nucleon K^- captures. The mass distributions of the two protons are shown in Fig. 2. A Gaussian fit of the peaks (neglecting the energy loss tails) is

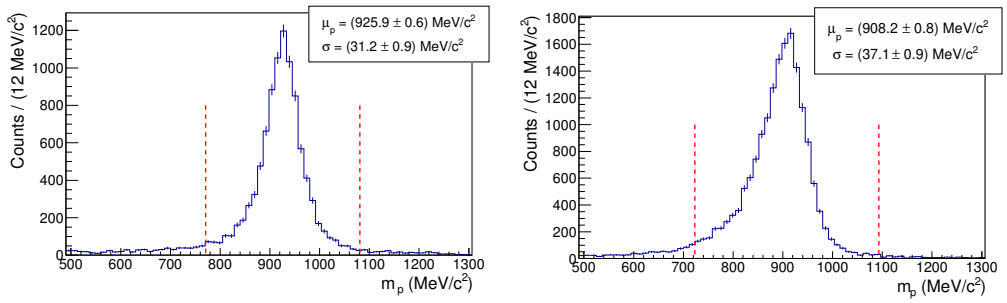

Figure 2: Mass of the proton from the Λ decay (left) and the primary proton mass (right) measured by TOF. The red dashed lines represent the applied cut.

performed and the cut $m_{\rm p} = (\mu_{\rm p} \pm 5\sigma)$ is applied for the selection of the final protons samples ($\mu_{\rm p}$ and σ represent the mean value and the standard deviation obtained from the fit and are reported in Fig. 2). The mean value of the two mass distributions is smaller than the nominal mass of the proton as a consequence of energy loss effect. Such effect is more pronounced for the primary protons since they are produced in the DC wall while, on contrary, most of the Λs decay within the DC volume.

In order to measure the mass of the protons by TOF both protons must have an associated cluster in the calorimeter. Since the energy threshold of the KLOE calorimeter corresponds to a proton momentum of about 240 MeV/c, larger than the Fermi momentum in ^{12}C, the contamination of pionic processes is reduced to 2 % in the final Λp sample. The contribution of single nucleon absorption processes will not be considered in the fit, but will be taken into account into the systematic errors. The comparison between the Λp invariant mass and proton momentum distributions of the $\Lambda {\rm p}\pi^-$ and the total Λp sample, after the selection of the protons by using the TOF is shown in Fig. 3.

3 % of the events belonging to the lower region of the proton momentum distribution ($p_{\rm p} < 270$ MeV/c) were removed in order to avoid biases due to the calorimeter threshold for low energy protons.

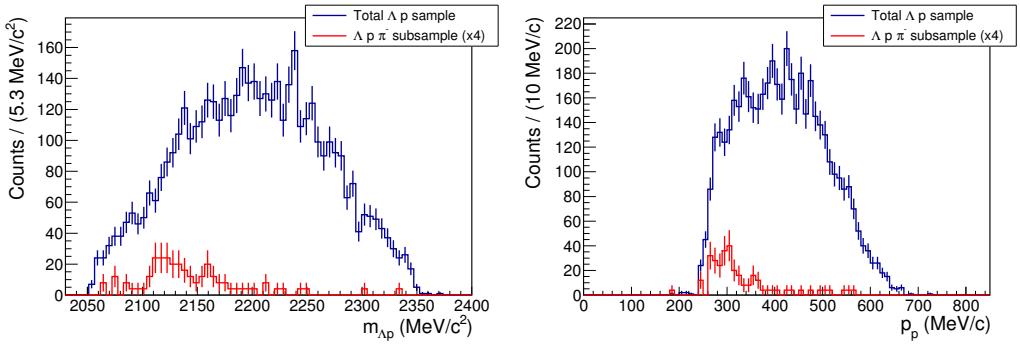

Figure 3: Λp invariant mass (left) and proton momentum (right) distributions after the selection of the protons from the mass by TOF are shown for the whole Λp data sample (blue) together with the $\Lambda p\pi^-$ subsample events (red). The red distribution is multiplied by a factor 4 for a more clear comparison.

In order to extract the BRs and the cross sections of the K^- multi-nucleon absorption processes, the final event selection has been performed also requiring the tagging of the K^- through the detection of a K^+ in the opposite hemisphere of the KLOE detector.

The final number of reconstructed Λp events is 4543, which was then analysed.

4. Monte Carlo simulations

The processes which contribute to Λp production in the final state of K^- absorptions in ^{12}C are simulated with the aim to fit the measured distributions in order to extract the corresponding BRs and cross sections. Beside the direct Λ production in the final state, also the primary Σ^0 production followed by the $\Sigma^0 \to \Lambda\gamma$ electromagnetic decay, as well as the primary Σ production followed by the Σ/Λ conversion processes, have to be taken into account.

The 2NA, 3NA and 4NA processes reported in Eqs. (1-3) are simulated both in the Λp and Σ^0p channels. Two separated contributions for the 2NA are considered: 1) the quasi-free (QF) production of the $\Lambda(\Sigma^0)$p pairs, without FSIs with the residual nucleus; 2) the primary $\Lambda(\Sigma^0)$N production followed by FSIs (only single collisions of the hyperon or the nucleon with the bound nucleons in the residual nucleus are accounted for).

For the 2NA-QF the following reactions are considered:

a) $K^- + {}^{12}C \rightarrow K^- +$ "pp" $+ R \rightarrow \Lambda + p + R$;

b) $K^- + {}^{12}C \rightarrow K^- +$ "pp" $+ R \rightarrow \Sigma^0 + p + R'$;

where R = $\{{}^{10}$Be, $2{}^4$He + 2n, ^{4}He + ^{3}H, ^{4}He + ^{3}He + 3n$\}$ and R$'$ = $\{{}^{10}$Be, $2{}^4$He + 2n, ^{4}He + 2p + 4n, 4p + 6n$\}$, corresponding to the cases with and without fragmentation of the residual ^{10}Be. For the Σ^0p channel the same reactions as in Ref. [40] are used. The relative amplitudes of these contributions are left free in the global fit. One further source of final Λp pair production considered is the Σ/Λ conversion process. The Σs produced in the primary K^- 2NA undergo further collisions with the Fermi sea residual nucleons remaining from the primary interaction, according to the elementary reaction $\Sigma N \rightarrow \Lambda N'$.

The kinematics of each process, defined by the hyperon Y (the Λ or the Σ^0) and the proton vector momenta ($\boldsymbol{p}_{\rm Y}, \boldsymbol{p}_{\rm p}$) are generated by sampling the total hyperon-proton momentum ($\boldsymbol{p}_{\rm Yp}$) distribution $P(\boldsymbol{p}_{\rm Yp})$, applying energy and momentum conservation.

The ($\boldsymbol{p}_{\rm Y}, \boldsymbol{p}_{\rm p}$) pair represents the input for the GEANFI digitisation followed by the event reconstruction. The momentum distributions are obtained following the phenomenological K^- absorption model described in Refs. [69, 70]:

$$P(p_{\rm Yp})\mathrm{d}p_{\rm Yp} = |\mathrm{T}(m_{\rm Yp})|^2 \cdot |\mathrm{F}(p_{\rm Yp})|^2 \cdot \mathrm{d}\rho \ , \tag{5}$$

the (unknown) energy dependence of the K^- multi-nucleon absorptions transition amplitudes (T($m_{\rm Yp}$)) is neglected, T($m_{\rm Yp}$) is then assumed uniform, the value has to be determined experimentally from the fit. F($p_{\rm Yp}$) is the form-factor containing "all" the nuclear physics, defined as in Ref. [69] replacing the single proton wave function with the two, three and four nucleons wave function for the 2NA, 3NA and 4NA processes, respectively. dρ is the phase space element and includes also the recoil of the residual nucleus. Gaussian wave functions are used for nucleons bound in the ^{12}C nucleus to calculate F($p_{\rm Yp}$), according to Refs. [71, 72]. The wave function of the K^- depends on the absorption process. For the at-rest K^- capture the kaons are assumed to be absorbed from the 2p atomic level in ^{12}C according to [43]. For the in-flight K^- capture the wave function adopted in Ref. [70] is used.

In the simulations the same amount of K^- captures at-rest and in-flight is considered, based on the analysis of the $\Lambda\pi^-$ correlated production, in which the two processes were clearly disentangled and found to equally contribute

to the final measured sample [73]. The error introduced by this assumption was included as a contribution to the systematic errors. The modulus of the K^- momentum, used to simulate the in-flight captures, is sampled according to the measured momentum distribution at the last point of the K^- track when the hadronic absorption occurs and a Λ is detected, according to the selection described in Section 2.

5. Fit of the data

The function used in the fit to model the measured kinematic distributions is taken as a linear combination of the MC components for the contributing processes previously described in Section 4, and assumes the following expression:

$$\mathcal{F}^q(q_n) = \sum_{i=1}^{N_{par}} \alpha_i \cdot h_i^q(q_n) \ , \tag{6}$$

where α_is are the free parameters of the fit, h_i^q represent the distribution of the kinematic variable q, corresponding to the i-th process, normalised to the data entries, N_{par} is the total number of parameters and q_n is the n-th bin for the variable q.

A simultaneous χ^2 fit of the Λp invariant mass ($m_{\Lambda \mathrm{p}}$), Λp angular correlation ($\cos\theta_{\Lambda \mathrm{p}}$), Λ momentum (p_Λ) and proton momentum (p_p) is performed using the SIMPLEX, MIGRAD and MINOS routines of ROOT [74, 75, 76] for the minimisation procedure. The result of the fit is shown in Fig. 4. Black points represent the data, black error bars correspond to the statistical errors and cyan error bars correspond to the systematic errors obtained according to the procedure that will be described in Section 6. The gray line distributions represent the global fitting functions, the coloured distributions represent the various contributing processes and their widths correspond to the statistical error. The reduced chi-squared is $\chi^2/dof = 194/206 = 0.94$.

For the evaluation of BRs and cross sections of the various processes the corresponding detection efficiencies, obtained on the basis of the MC simulations, are used. The larger efficiencies are obtained for the 2NA-QF and for the 3NA. The efficiency of the 2NA-QF is found to be (2.49 ± 0.02) % in the Λp channel and (1.24 ± 0.26) % in the Σ^0p channel, while those of the 3NA are (1.77 ± 0.01) % and (0.65 ± 0.01) %, respectively. The detection efficiency is energy dependent and increases with the track momentum, thus it is higher for the K^- 2NA-QF in the Λp channel since the protons are

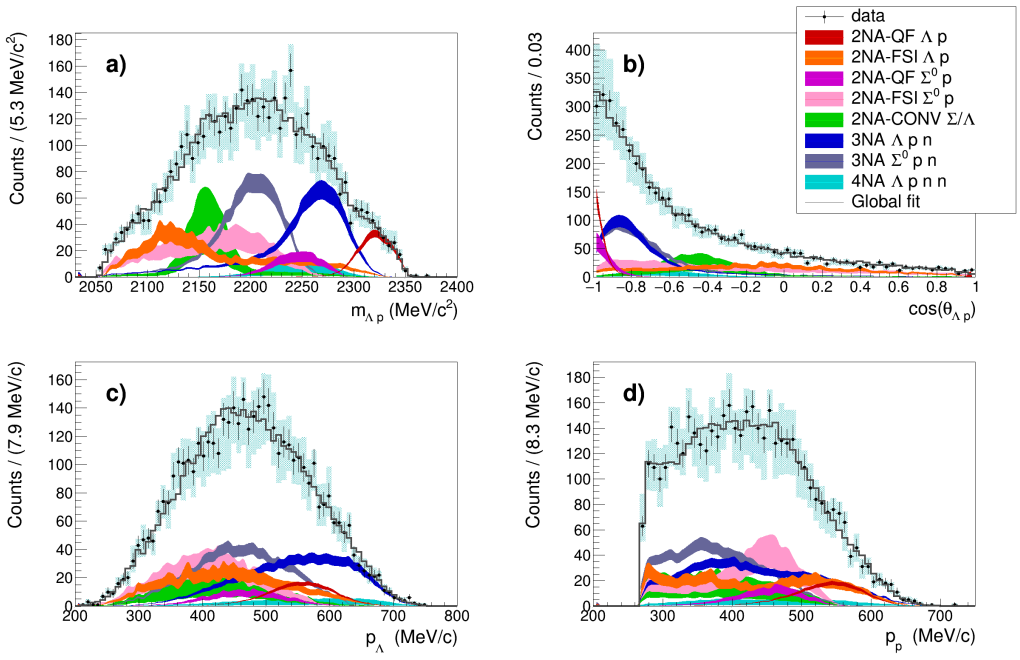

Figure 4: Λp invariant mass (panel a), Λp angular correlation (panel b), Λ momentum (panel c) and proton momentum (panel d) distributions are reported for the K^- absorption on ^{12}C listed in the legend. Black points represent the data, black error bars correspond to the statistical errors, cyan error bars correspond to the systematic errors. The gray line distributions represent the global fitting functions, the coloured distributions represent the different contributing processes according to the colour code reported in the legend and the widths correspond to the statistical error.

emitted with a larger mean momentum with respect to the other processes, as shown in Fig. 4. The obtained efficiencies are lower than 3% due to the protons selection using the mass by TOF. The measurement of the TOF, indeed, requires the energy cluster association in the calorimeter for the two proton tracks, reducing the amount of selected events.

The BR for the process i is defined as

$$BR_i = \frac{N_i^{at-rest}}{N_{K^-stop}} \ , \tag{7}$$

where $N_i^{at-rest}$ represents the absolute number of events for the i absorption process when the K^- is captured at-rest, obtained from the corresponding contribution to the fit corrected by the detection efficiency; N_{K^-stop} is the

number of stopped K^- in the DC entrance wall for the analysed luminosity which have been tagged through the detection of a K^+, emitted in the opposite hemisphere of the KLOE detector.

The cross sections are evaluated as

$$\sigma_{\rm i} = \frac{{\rm N}_{\rm i}^{\rm in-flight}}{{\rm N}_{\rm K^-}^{\rm projectiles} \cdot {\rm n} \cdot {\rm L}} \ , \tag{8}$$

where $\mathrm{N}_{\mathrm{i}}^{\mathrm{in-flight}}$ represents the absolute number of events for the i absorption process when the K^- is captured in-flight, obtained from the corresponding contribution to the fit corrected by the detection efficiency; $\mathrm{N}_{\mathrm{K^-}}^{\mathrm{projectiles}}$ is the number of K^- impinging on the DC entrance wall for the analysed luminosity which have been tagged; n is the density of the interaction centres of the target material and L is the thickness of the Carbon wall. The obtained BRs and cross sections are summarised in Table 1. The K^- momentum at which the cross section is measured is evaluated in the centre of mass reference frame of the absorbing nucleons, thus it differs for the 2NA and 3NA processes.

Table 1: Branching ratios (for the K^- absorbed at-rest) and cross sections (for the K^- absorbed in-flight) of the K^- multi-nucleon absorption processes. The K^- momentum is evaluated in the centre of mass reference frame of the absorbing nucleons, thus it differs for the 2NA and 3NA processes. The statistical and systematic errors are also given.

Process	Branching Ratio (%)	σ (mb)	@	p_K (MeV/c)
2NA-QF Λp	0.25 ± 0.02 (stat.) $^{+0.01}_{-0.02}$(syst.)	2.8 ± 0.3 (stat.) $^{+0.1}_{-0.2}$ (syst.)	@	128 ± 29
2NA-FSI Λp	6.2 ± 1.4(stat.) $^{+0.5}_{-0.6}$(syst.)	69 ± 15 (stat.) ± 6 (syst.)	@	128 ± 29
2NA-QF Σ^0p	0.35 ± 0.09(stat.) $^{+0.13}_{-0.06}$(syst.)	3.9 ± 1.0 (stat.) $^{+1.4}_{-0.7}$ (syst.)	@	128 ± 29
2NA-FSI Σ^0p	7.2 ± 2.2(stat.) $^{+4.2}_{-5.4}$(syst.)	80 ± 25 (stat.) $^{+46}_{-60}$ (syst.)	@	128 ± 29
3NA Λpn	1.4 ± 0.2(stat.) $^{+0.1}_{-0.2}$(syst.)	15 ± 2 (stat.) ± 2 (syst.)	@	117 ± 23
3NA Σ^0pn	3.7 ± 0.4(stat.) $^{+0.2}_{-0.4}$(syst.)	41 ± 4 (stat.) $^{+2}_{-5}$ (syst.)	@	117 ± 23
4NA Λpnn	0.13 ± 0.09(stat.) $^{+0.08}_{-0.07}$(syst.)	-		
2NA-CONV Σ/Λ	2.1 ± 1.2(stat.) $^{+0.9}_{-0.5}$(syst.)	-		

6. Systematic errors

The systematic uncertainties for the measurements are obtained by performing variations of each cut applied for the Λp event selection described in Section 3. The systematic error to the parameter α_i introduced by the variation of the j-th cut is given by:

$$\sigma^j_{sist.,i} = \alpha^j_i - \alpha_i \ , \tag{9}$$

where α_i^j is the value obtained from the new fit. The total, positive and negative, systematic errors are obtained summing in quadrature, separately, the positive and negative systematics.

In Table 2, the standard selection cuts for the kinematic variables which are found to significantly contribute to the systematic errors are summarised. The $\rho_{\Lambda p}$ cut variations are performed in order to select $\pm 15\%$ of events,

Table 2: Cuts of the optimised Λp event selection that significantly contribute to the systematic errors.

Hadronic vertex radial coordinate:	23.8 cm $< \rho_{\Lambda p} <$ 26.2 cm
Extra-proton mass:	723 MeV/c^2 $< m_p <$ 1093 MeV/c^2
Proton from the Λ decay mass:	771 MeV/c^2 $< m_p <$ 1081 MeV/c^2
Proton momentum:	$p_p \geq$ 270 MeV/c

for the proton TOF mass cuts we relied on the standard deviation of the mass distribution fits ($\pm 2\sigma$) and the systematic on the proton momentum cut is evaluated by removing it. Two important additional contributions to the systematic errors are also considered, related to the assumptions of the event modelling, namely the ansatz on the equal in-flight/at-rest contribution, which is varied to 40/60% and 60/40%, and the contribution of the single nucleon absorptions, evaluated performing the fit with additional pionic contributions.

7. Discussion of the results

7.1. K^- multi-nucleon absorption BRs and cross sections

The BRs and cross sections of the 2NA-QF and of the 3NA with the production of the Λ and the Σ^0 in the final state are obtained with a better precision with respect to the other components, as it is evident from Fig. 4 and Table 1. For these processes the relative error (combined statistical and systematic) on the measured yields is smaller than 20% except for the 2NA-QF Σ^0p.

The fit is not sensitive to the contribution of the 4NA process due to the overlap with the 3NA over a broad range of the phase space (compare for example the invariant mass distributions in Fig. 4); moreover the 4NA Λp production is strongly uncorrelated, similar to FSI or conversion processes

(as evident from the $\cos\theta_{\Lambda p}$ spectra). Consequently, is not possible to pin down the 4NA with enough accuracy. The 2NA-QF component with the direct Λp production is clearly disentangled from the other contributions, especially in the Λp invariant mass distribution. The 3NA can also be well identified and is measured with unprecedented accuracy for both the Λp and Σ^0p channels. The global branching ratio of the K^- multi-nucleon absorptions in ^{12}C producing $\Lambda(\Sigma^0)$p final states, obtained summing all the BRs of Table 1, is found to be consistent with the bubble chamber measurements reported in Refs. [29, 32].

7.2. K^-p coupling to the $\Lambda(1405)$

Considering the meson exchange model, the processes K^-"pp" $\rightarrow \Lambda$p and K^-"pp" $\rightarrow \Sigma^0$p occur with the exchange of a π^0 (see Ref. [77]) according to the diagrams shown in Fig. 5.

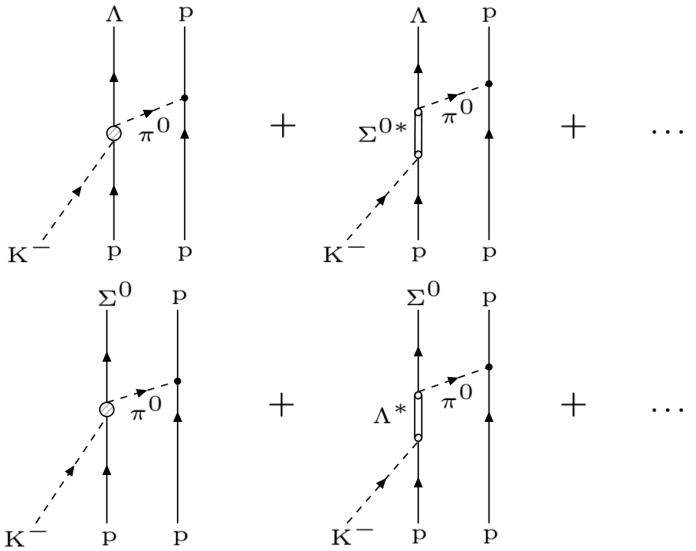

Figure 5: The tree level (left) and the leading order (right) diagrams of the processes K^-"pp" $\rightarrow \Lambda$p (top) and K^-"pp" $\rightarrow \Sigma^0$p (bottom), according to the meson exchange model.

As a consequence, the ratio of the BRs of the 2NA-QF Λp and the 2NA-QF Σ^0p is directly related to the ratio of BRs of the K^-"p" $\rightarrow \Lambda\pi^0$ and the

K^- "p" $\rightarrow \Sigma^0\pi^0$ processes:

$$\mathcal{R} = \frac{\mathrm{BR}(K^- \text{“pp”} \rightarrow \Lambda p)}{\mathrm{BR}(K^- \text{“pp”} \rightarrow \Sigma^0 p)} = \frac{\mathrm{BR}(K^- \text{“p”} \rightarrow \Lambda\pi^0)}{\mathrm{BR}(K^- \text{“p”} \rightarrow \Sigma^0\pi^0)} \ . \tag{10}$$

The exchange of a K^- meson is also possible [78, 79, 80]. Detailed calculations dating from the emulsion studies period show that the effect of the latter is a 30% correction to the pion exchange [78]. Nevertheless, the two mechanisms add coherently and equation (10) still holds. Given that the $\Lambda\pi^0$ and $\Sigma^0\pi^0$ production below the $\bar{K}N$ threshold involve the intermediate formation of the $\Sigma^0(1385)$ and $\Lambda(1405)$ resonances, the measured ratio gives information on the complex and debated properties of these resonances.

Using the branching ratios in Table 1 we measure:

$$\mathcal{R} = 0.7 \pm 0.2(\mathrm{stat.})^{+0.2}_{-0.3}(\mathrm{syst.}) \ . \tag{11}$$

This ratio is to be compared with the ratio $\mathcal{R}'$ between the phase spaces of the two reactions:

$$K^- + {}^{12}C \rightarrow K^- + \text{“pp”} + R \rightarrow \Lambda + p + R \tag{12}$$

and

$$K^- + {}^{12}C \rightarrow K^- + \text{“pp”} + R' \rightarrow \Sigma^0 + p + R' \ , \tag{13}$$

which is given by:

$$\mathcal{R}' = \frac{\sum_R \cdot w_R \cdot \int |F(p_{\Lambda p})|^2 \cdot d\rho_{\Lambda p}}{\sum_{R'} \cdot w_{R'} \cdot \int |F(p_{\Sigma^0 p})|^2 \cdot d\rho_{\Sigma^0 p}} = 1.22 \ . \tag{14}$$

The sum is performed over residual nuclei combinations considered in the fit, where w_R and $w_{R'}$ are the relative weights extracted from the fit.

By comparing (11) with (14) we see that the resonance dynamics dominates over the pure phase spaces, mirroring the isospin I=0 $\Lambda(1405)$ cross section dominance over the I=1 $\Sigma^0(1385)$ cross section. This measurement provides crucial information on the $\Lambda(1405)$ in medium properties and on the resonance couplings to the $\bar{K}N$ and $\Sigma\pi$ channels.

7.3. Search for a K^-pp Bound State

In the following, a contribution of a K^-pp bound state to the measured Λp distributions is investigated. The K^-pp bound state formation in Carbon

$$K^- + {}^{12}C \rightarrow K^-pp + {}^{10}Be \rightarrow \Lambda + p + {}^{10}Be \ , \tag{15}$$

followed by the K^-pp decay in Λp, was simulated according to the procedure described in Section 4, using a Breit-Wigner shape for $|T(m_{\Lambda p})|^2$.

In order to test the sensitivity of the experimental spectra to an eventual K^-pp signal, the kinematic shapes of the K^-"pp" 2NA process are compared with bound states simulations, selecting for the bound state values for binding energies and widths which are claimed in previous experimental findings: E15, E27, FINUDA, DISTO and OBELIX, listed in Table 3. In the case of OBELIX the upper limit for the bound state width is used.

Table 3: Experimental BE and Γ of the K^-pp bound state measured by the FINUDA, OBELIX, DISTO, E27 and E15 experiments.

Experiment	BE (MeV)	Γ (MeV/c^2)
FINUDA [33]	$115\ ^{+6}_{-5}$ (stat.) $^{+3}_{-4}$ (syst.)	$67\ ^{+14}_{-11}$ (stat.) $^{+2}_{-3}$ (syst.)
OBELIX [34]	160.9 ± 4.9	$< 24.4 \pm 8.0$
DISTO [36]	103 ± 3 (stat.) ± 5 (syst.)	118 ± 8 (stat.) ± 10 (syst.)
E27 [39]	$95\ ^{+18}_{-17}$ (stat.) $^{+30}_{-21}$ (syst.)	$162\ ^{+87}_{-45}$ (stat.) $^{+66}_{-78}$ (syst.)
E15 [41]	$15\ ^{+6}_{-8}$ (stat.) ± 12 (syst.)	$110\ ^{+19}_{-17}$ (stat.) ± 27 (syst.)

The calculated Λp invariant mass distributions, corresponding to the parameters listed in Table 3, are shown in Fig. 6, together with the shapes for the K^-"pp" 2NA absorption process.

The comparative study evidences that, for low-energy K^- absorption in ^{12}C, a bound state characterised by the quoted parameters can not be distinguished from the 2NA.

In order to further test the experimental sensitivity to the width of the bound state, the same kinematic distributions where calculated for a fixed binding energy (BE=45 MeV) and various widths (Γ = 5, 15, 30, 50 and 90 MeV/c^2). The invariant mass shapes are shown in Fig. 7. It emerges that a bound state signal could be disentangled by the 2NA only for extremely narrow states ($\Gamma < 15$ MeV/c^2), excluded by theoretical predictions [4, 5, 6, 7, 8, 9, 10, 11, 12, 13, 14]. The same result is obtained also for other choices of the BE.

The total branching ratio of the 2NA process decaying into Λp (QF and with FSIs) is measured to be:

$$BR(K^-2NA \to \Lambda p) = (6.5 \pm 1.2(stat.)^{+0.5}_{-0.6}(syst.))\% \ , \qquad (16)$$

and it contains the K^-pp contribution, if such a state exists.

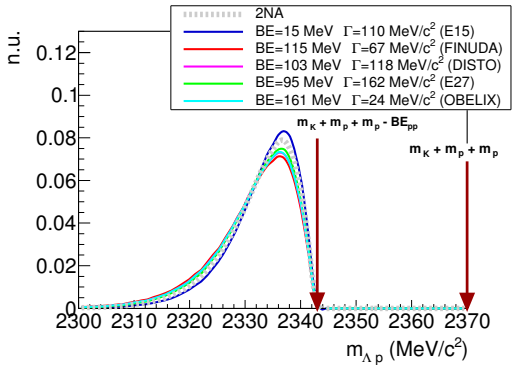

Figure 6: Calculated invariant mass distributions of the Λp pairs from the K^-pp bound state decay, produced in K^- absorption on ^{12}C. The line shape of the 2NA (gray line) is shown for comparison together with the shapes obtained for the simulation of a bound state having binding energy and width selected according to the measurements of E15 (blue line), FINUDA (red line), DISTO (magenta line), E27 (green line) and OBELIX (cyan line). The areas of the distributions are normalised to unity.

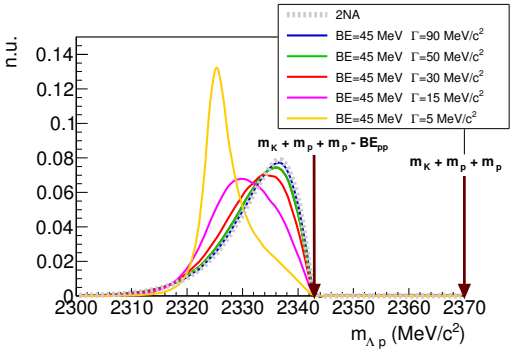

Figure 7: Calculated Λp invariant mass distributions for the process $K^- + {}^{12}C \to K^-pp + {}^{10}Be \to \Lambda + p + {}^{10}Be$, for a bound state having BE = 45 MeV and Γ = 5, 15, 30, 50 and 90 MeV/c^2 (yellow, magenta, red, green and blue curves respectively). The gray curve is the shape of the 2NA-QF. The areas of the distributions are normalised to unity.

7.4. Comparison with the FINUDA result

It is interesting to compare our Λp invariant mass spectrum with the one measured by FINUDA [33], which is interpreted as a K^-pp bound state decay. The target used in Ref. [33] is a mixture of ^{12}C, ^{6}Li and ^{7}Li, in the following proportions: 51 %, 35 % and 14 % respectively. In Ref. [43] is, however, demonstrated that the ^{12}C component dominates. This is motivated by the

larger amount of protons, the higher probability of the FSI in the bigger nucleus and by the larger overlap with the K^- wave function. In order to perform a direct comparison we included in our selection the same angular distribution cut which was performed in Ref. [33] to pin down the back-to-back Λp production, which is argued in Ref. [33] to be directly correlated to the K^-pp bound state production:

$$\cos\theta_{\Lambda p} < -0.8 \ . \tag{17}$$

The obtained Λp invariant mass spectrum is shown in Fig. 8.

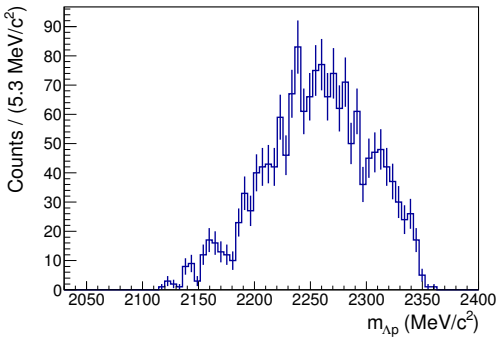

Figure 8: The experimental Λp invariant mass spectrum obtained selecting back-to-back Λp events ($\cos\theta_{\Lambda p} < -0.8$), in analogy with the data analysis performed by FINUDA in Ref [33].

The shape of the Λp invariant mass spectrum in Fig. 8 is compatible with the corresponding spectrum reported by the FINUDA collaboration in Fig. 3 of Ref. [33]. Performing the simultaneous fit of the Λp invariant mass, the Λp angular correlation, the Λ and the proton momenta, in complete analogy with the procedure described for the fit of our complete selected Λp data sample, a reduced χ^2 of $\chi^2/ndf = 123/130 = 0.94$ is obtained. The result of the fit is shown in detail for the invariant mass and proton momentum components in Fig. 9.

The BRs per stopped K^- of the various contributing processes are again evaluated using the parameters obtained from the fit of the back-to-back Λp events and are presented in Table 4. The BRs are compatible with those obtained from the fit of the full selected data sample reported in Table 1, in both cases the measured distributions can be well explained in terms of K^- multi-nucleon absorption processes. The fit to the back-to-back Λp sample

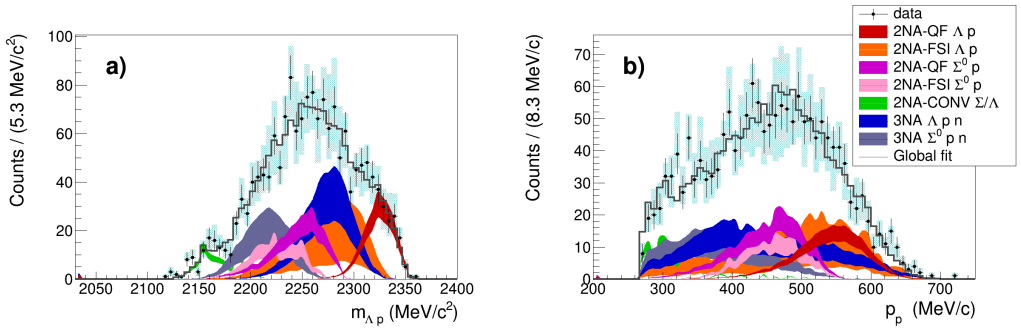

Figure 9: Λp invariant mass (panel a) and proton momentum (panel b) spectra. Black points represent the data, black error bars correspond to the statistical errors, cyan error bars correspond to the systematic errors. The gray line distributions represent the global fitting functions. The color legend for the different contributing processes is shown in the figure.

Table 4: The branching ratios of K^- the multi-nucleon absorptions for a back-to-back (a la FINUDA) selection of Λ and p are reported together with the statistical and systematic errors.

Process	Branching Ratio (%)
2NA-QF Λp	$0.20 \pm 0.04(\text{stat.}) \pm 0.02(\text{syst.})$
2NA-FSI Λp	$3.8 \pm 2.3(\text{stat.}) \pm 1.1(\text{syst.})$
2NA-QF Σ^0p	$0.54 \pm 0.20(\text{stat.}) \,^{+0.20}_{-0.16}(\text{syst.})$
2NA-FSI Σ^0p	$5.4 \pm 1.5(\text{stat.}) \,^{+1.0}_{-2.7}(\text{syst.})$
3NA Λpn	$1.1 \pm 0.3(\text{stat.}) \pm 0.2(\text{syst.})$
3NA Σ^0pn	$1.9 \pm 0.7(\text{stat.}) \,^{+0.8}_{-0.4}(\text{syst.})$
2NA-CONV Σ/Λ	$22 \pm 4(\text{stat.}) \,^{+1}_{-12}(\text{syst.})$

is not sensitive to the contribution of the Σ/Λ conversion process which is the most critically affected by the additional phase space cut as evidenced by the big systematic error.

Concluding, even imposing the back-to-back angular selection to pin down a highly correlated Λp production, the spectrum can be completely explained in terms of K^- multi-nucleon absorption processes, without the need of a K^-pp component, whose partial contribution, if any, is contained in the 2NA.

8. Summary

In this work the correlated Λp pairs production from low-energy K^- ^{12}C absorption was investigated, taking advantage of the negatively charged kaons produced by ϕ decaying at-rest at the DAΦNE collider. A sample of almost pure K^- ^{12}C interactions is obtained by selecting the K^- captures in the inner wall of the KLOE drift chamber, which is used as an active target. The key selection criterion which characterises the Λp correlated pairs production search, presented in this work, is represented by the measurement of the mass by time of flight for both the involved protons. One proton is originated in the $\Lambda \to p\pi^-$ decay, one is produced at the K^- multi-nucleon absorption. At the price of a reduced statistics this selection returns an extremely clean data sample. The acceptance cut which results from the protons detection in the calorimeter (necessary for the time of flight measurement) suppresses the K^- single nucleon absorption (1NA) contributions. The calorimeter momentum threshold ($p > 240$ MeV/c) is indeed higher than the typical momentum of protons emerging from pionic productions. The residual 1NA contamination, surviving the selection cuts, is considered as a contribution to the systematic errors.

BRs and cross sections of the K^- multi-nucleon absorptions on two, three and four nucleons (2NA, 3NA and 4NA) were obtained by means of a simultaneous fit of the Λp invariant mass, Λp angular correlation, Λ and proton momenta to the simulated distributions for both direct Λ production and Σ^0 production followed by $\Sigma^0 \to \Lambda\gamma$ decay. The K^- nuclear capture was calculated for both atomic and flight interactions. In the first case the absorption from atomic 2p state is assumed. Fragmentations of the residual nucleus following the hadronic interaction were also considered. For the 2NA the important contributions of both final state interactions (FSI) of the Λ and the proton were taken into account, as well as the conversion of primary produced sigma particles ($\Sigma N \to \Lambda N'$), this allows to disentangle the quasi-free (QF) production. The global branching ratio for the K^- multi-nucleon absorptions in ^{12}C (with $\Lambda(\Sigma^0)$p final states) is found to be compatible with bubble chamber and emulsion results.

The Λp direct production in 2NA-QF is phase space favoured with respect to the corresponding Σ^0p final state. The ratio among the Λp direct production in 2NA-QF and the corresponding Σ^0p production is found to be $0.7 \pm 0.2(\text{stat.})^{+0.2}_{-0.3}(\text{syst.})$. Given that the ratio between the final state phase spaces for the two processes is $\mathcal{R} \simeq 1.22$, the dominance of the Σ^0p channel

is a clear contribution of the $\Lambda(1405)$, from which to extract information on the $\bar{K}N$ dynamics below threshold.

The last part of this work is devoted to the search for K^-pp bound state contribution to the measured Λp production. The simulated distributions were obtained in agreement with the multi-nucleon K^- capture calculation assuming a Breit-Wigner distribution for the bound state formation transition amplitude. The 2NA-QF is found to completely overlap with the K^-pp, except for small values of the bound state width of the order of 15 MeV/c^2 or less. A further selection of back-to-back Λp production was performed by selecting $\cos\theta_{\Lambda p} < -0.8$ in order to make a direct comparison with the corresponding FINUDA measurement. The shape of the invariant mass distribution is perfectly compatible with the shape presented in Ref. [33]. By repeating the fitting procedure the spectra result to be completely described in terms of K^- multi-nucleon absorption processes, the BRs are compatible with those obtained from the fit of the full data sample, with no need of a K^-pp component, whose partial contribution, if any, is contained in the 2NA.

Acknowledgements

We acknowledge the KLOE/KLOE-2 Collaboration for their support and for having provided us the data and the tools to perform the analysis presented in this paper. Part of this work was supported by Minstero degli Affari Esteri e della Cooperazione Internazionale, Direzione Generale per la Promozione del Sistema Paese (MAECI), Strange Matter project PRG00892; Polish National Science Center through grant No. UMO-2016/21/D/ST2/01155.

References

[1] C. Fuchs, Kaon production in heavy ion reactions at intermediate energies, Prog. Part. Nucl. Phys. 53 (2004) 113–124.

[2] W. Weise, Topics in low-energy QCD with strange quarks, Hyperfine Interact. 233 (2015) 131–140.

[3] F. Weber, et al., Strangeness in Neutron Stars, Int. J. Mod. Phys. D16 (2007) 231–245.

[4] Y. Akaishi, T. Yamazaki, Nuclear anti-K bound states in light nuclei, Phys. Rev. C65 (2002) 044005.

[5] Y. Ikeda, T. Sato, Strange dibaryon resonance in the $\bar{K}$NN - πYN system, Phys. Rev. C76 (2007) 035203.

[6] N. V. Shevchenko, A. Gal, J. Mares, Faddeev calculation of a K^-pp quasi-bound state, Phys. Rev. Lett. 98 (2007) 082301.

[7] S. Wycech, A. Green, Variational calculations for K^- few-nucleon systems, Phys. Rev. C79 (2009) 014001.

[8] J. Révai, N. V. Shevchenko, Faddeev calculations of the $\bar{K}$NN system with chirally motivated $\bar{K}$N interaction. II. The K^-pp quasibound state, Phys.Rev. C90 (2014) 034004.

[9] S. Maeda, Y. Akaishi, T. Yamazaki, Strong binding and shrinkage of single and double kbar nuclear systems (K^-pp, K^-ppn, K^-K^-p and K^-K^-pp) predicted by Faddeev-Yakubovsky calculations, Proc. Jpn. Acad. B 89 (2013) 418.

[10] A. Dote, T. Hyodo, W. Weise, Variational calculation of the ppK^- system based on chiral SU(3) dynamics, Phys. Rev. C79 (2009) 014003.

[11] N. Barnea, A. Gal, E. Liverts, Realistic calculations of $\bar{K}$NN, $\bar{K}$NNN, and $\bar{K}\bar{K}$NN quasibound states, Phys. Lett. B712 (2012) 132–137.

[12] Y. Ikeda, H. Kamano, T. Sato, Energy dependence of $\bar{K}$N interactions and resonance pole of strange dibaryons, Prog. Theor. Phys. 124 (2010) 533–539.

[13] P. Bicudo, Microscopic 8-quark study of the antikaon-nucleon-nucleon systems, Phys. Rev. D76 (2007) 031502.

[14] M. Bayar, E. Oset, The $\bar{K}$NN system revisited including absorption, Nucl. Phys. A914 (2013) 349–353.

[15] G. Abrams, B. Sechi-Zorn, Charge-Exchange Scattering of Low-Energy K^- Mesons in Hydrogen, Phys. Rev. 139 (1965) B454.

[16] M. Sakitt, et al., Low-energy K^- Meson Interactions In Hydrogen, Phys. Rev. 139 (1965) B719.

[17] J. Kim, Low Energy K^--p Interaction of the 1405-MeV Y_0^* Resonance as $\bar{K}$N Bound State, Phys. Rev. Lett. 14 (1965) 29.

[18] M. Csejthey-Barth, et al., The interactions of low energy K^- mesons with protons, Phys. Lett. 16 (1965) 89.

[19] T. Mast, et al., Elastic, Charge Exchange, and Total K^-p Cross-Sections in the Momentum Range 220 to 470 MeV/c, Phys. Rev. D14 (1976) 13.

[20] R. Bangerter, et al., Reactions $K^-p \to \Sigma^-\pi^+$ and $K^-p \to \Sigma^+\pi^-$ in the momentum range from 220 to 470 MeV/c, Phys. Rev. D23 (1981) 1484.

[21] J. Ciborowski, et al., Kaon Scattering And Charged Sigma Hyperon Production In K^-p Interactions Below 300 MeV/c, J. Phys. G8 (1982) 13.

[22] D. Evans, et al., Charge Exchange Scattering In K^-p Interactions Below 300 MeV/c, J. Phys. G9 (1983) 885.

[23] W. E. Humphrey, R. R. Ross, Low-Energy Interactions of K^- Mesons in Hydrogen, Phys. Rev. 127 (1962) 1305.

[24] J. K. Kim, Report NEVIS-149, Columbia University (1966).

[25] M. Bazzi, et al., A new measurement of kaonic hydrogen X-rays, Phys. Lett. B704 (2011) 113.

[26] M. Bazzi, et al., Measurements of the strong-interaction widths of the kaonic ^{3}He and ^{4}He 2p levels, Phys. Lett. B714 (2012) 40.

[27] M. Bazzi, et al., Preliminary study of kaonic deuterium X-rays by the SIDDHARTA experiment at DAFNE, Nucl. Phys. A907 (2013) 69–77. arXiv:1302.2797, doi:10.1016/j.nuclphysa.2013.03.001.

[28] M. Bazzi, et al., K-series X-ray yield measurement of kaonic hydrogen atoms in a gaseous target, Nucl. Phys. A954 (2016) 7–16. arXiv:1603.00094, doi:10.1016/j.nuclphysa.2016.03.047.

[29] P. A. Katz, et al., Reactions of stopping K^- in helium, Phys. Rev. D1 (1970) 1267–1276. doi:10.1103/PhysRevD.1.1267.

[30] H. Davis, et al., A bubble chamber study of the reactions occurring with stopping K^--mesons in a mixture of propane and freon, Nuov. Cim. A53 (1968) 313–326.

[31] J. W. Moulder, et al., K^- meson absorption in neon, Nucl. Phys. B35 (1971) 332–350. doi:10.1016/0550-3213(71)90458-5.

[32] C. Vander Velde-Wilquet, et al., Determination of the Branching Fractions for K^- Meson Absorption at Rest in Carbon Nuclei, Nuovo Cim. A39 (1977) 538–547. doi:10.1007/BF02771028.

[33] M. Agnello, et al., Evidence for a kaon-bound state K^-pp produced in K^- absorption reactions at rest, Phys. Rev. Lett. 94 (2005) 212303. doi:10.1103/PhysRevLett.94.212303.

[34] G. Bendiscioli, et al., Search for signals of bound anti-K nuclear states in antiproton He-4 annihilations at rest, Nucl. Phys. A789 (2007) 222–242. doi:10.1016/j.nuclphysa.2007.03.010.

[35] T. Suzuki, et al., YN correlations from the stopped K^- reaction on He-4, Mod. Phys. Lett. A23 (2008) 2520–2523. arXiv:0711.4943, doi:10.1142/S021773230802971X.

[36] T. Yamazaki, et al., Indication of a deeply bound compact K^-pp state formed in the $pp \to p\Lambda K^+$ reaction at 2.85 GeV, Phys. Rev. Lett. 104 (2010) 132502. arXiv:1002.3526, doi:10.1103/PhysRevLett.104.132502.

[37] A. O. Tokiyasu, et al., Search for K^-pp bound state via $\gamma d \to k^+\pi^- X$ reaction at E_γ = 1.5-2.4 GeV, Phys. Lett. B728 (2014) 616–621. arXiv:1306.5320, doi:10.1016/j.physletb.2013.12.039.

[38] G. Agakishiev, et al., Partial Wave Analysis of the Reaction $p(3.5GeV) + p \to pK^+\Lambda$ to Search for the "ppK^-" Bound State, Phys. Lett. B742 (2015) 242–248. arXiv:1410.8188, doi:10.1016/j.physletb.2015.01.032.

[39] Y. Ichikawa, et al., Observation of the "K^-pp"-like structure in the $d(\pi^+, K^+)$ reaction at 1.69 GeV/c, PTEP 2015 (2) (2015) 021D01. arXiv:1411.6708, doi:10.1093/ptep/ptv002.

[40] O. Vázquez Doce, et al., K^- absorption on two nucleons and ppK^- bound state search in the $\Sigma^0 p$ final state, Phys. Lett. B758 (2016) 134–139. arXiv:1511.04496, doi:10.1016/j.physletb.2016.05.001.

[41] Y. Sada, et al., Structure near the K^- + p + p threshold in the in-flight ^{3}He(K^-, p)n reaction, PTEP 2016 (5) (2016) 051D01. arXiv:1601.06876, doi:10.1093/ptep/ptw040.

[42] S. Ajimura, et al., "K^-pp", a $\bar{K}$-Meson Nuclear Bound State, Observed in ^{3}He(K^-,Λp)n ReactionsarXiv:1805.12275.

[43] V. K. Magas, E. Oset, A. Ramos, H. Toki, A Critical view on the deeply bound K^-pp system, Phys. Rev. C74 (2006) 025206. arXiv:nucl-th/0601013, doi:10.1103/PhysRevC.74.025206.

[44] V. K. Magas, E. Oset, A. Ramos, Critical review of K^-ppn bound states, Phys. Rev. C77 (2008) 065210. arXiv:0801.4504, doi:10.1103/PhysRevC.77.065210.

[45] R. Barth, et al., Subthreshold production of kaons and anti-kaons in nucleus-nucleus collisions at equivalent beam energies, Phys. Rev. Lett. 78 (1997) 4007–4010. doi:10.1103/PhysRevLett.78.4007.

[46] P. Senger, et al., Kaon production in relativistic nucleus nucleus collisions, Acta Phys. Polon. B27 (1996) 2993–3004.

[47] F. Laue, et al., Medium effects in kaon and anti-kaon production in nuclear collisions at subthreshold beam energies, Phys. Rev. Lett. 82 (1999) 1640–1643. arXiv:nucl-ex/9901005, doi:10.1103/PhysRevLett.82.1640.

[48] A. Schroter, et al., Subthreshold anti-proton and K^- production in heavy ion collisions, Z. Phys. A350 (1994) 101–113. doi:10.1007/BF01290678.

[49] V. Zinyuk, et al., Azimuthal emission patterns of K^+ and of K^- mesons in Ni+Ni collisions near the strangeness production threshold, Phys. Rev. C90 (2) (2014) 025210. arXiv:1403.1504, doi:10.1103/PhysRevC.90.025210.

[50] P. Gasik, et al., Strange meson production in Al+Al collisions at 1.9 A GeV, Eur. Phys. J. A52 (6) (2016) 177. arXiv:1512.06988, doi:10.1140/epja/i2016-16177-y.

[51] K. Piasecki, et al., Centrality dependence of subthreshold ϕ meson production in Ni + Ni collisions at 1.9A GeV, Phys. Rev. C94 (1) (2016) 014901. arXiv:1602.04378, doi:10.1103/PhysRevC.94.014901.

[52] J. Adamczewski-Musch, et al., Deep sub-threshold ϕ production in Au+Au collisions, Phys. Lett. B778 (2018) 403–407. arXiv:1703.08418, doi:10.1016/j.physletb.2018.01.048.

[53] W. Scheinast, et al., First observation of in-medium effects on phase space distributions of antikaons measured in proton-nucleus collisions, Phys. Rev. Lett. 96 (2006) 072301. arXiv:nucl-ex/0512028, doi:10.1103/PhysRevLett.96.072301.

[54] A. V. Akindinov, et al., Subthreshold and near-threshold kaon and antikaon production in proton-nucleus reactions, J. Phys. G37 (2010) 015107. arXiv:0911.4616, doi:10.1088/0954-3899/37/1/015107.

[55] A. V. Akindinov, et al., Investigation of the subthreshold production of K^- mesons in proton-nucleus collisions, JETP Lett. 85 (2007) 142–148, [Pisma Zh. Eksp. Teor. Fiz.85,174(2007)]. doi:10.1134/S0021364007030034.

[56] A. V. Akindinov, et al., Experimental study of subthreshold K^- production in proton nucleus collisions and the calculation of this production in frame of the modern models.

[57] Yu. T. Kiselev, et al., Kaon pair production in proton-nucleus collisions at 2.83 GeV kinetic energy, Phys. Rev. C92 (2015) 065201. arXiv:1509.04830, doi:10.1103/PhysRevC.92.065201.

[58] A. Polyanskiy, et al., Measurement of the in-medium phi-meson width in proton-nucleus collisions, Phys. Lett. B695 (2011) 74–77. arXiv:1008.0232, doi:10.1016/j.physletb.2010.10.050.

[59] M. Hartmann, et al., Momentum dependence of the phi-meson nuclear transparency, Phys. Rev. C85 (2012) 035206. arXiv:1201.3517, doi:10.1103/PhysRevC.85.035206.

[60] M. Agnello, et al., Σ^-p emission rates in K^- absorptions at rest on ^{6}Li, ^{7}Li, ^{9}Be, ^{13}C and ^{16}O, Phys. Rev. C92 (4) (2015) 045204. arXiv:1508.00139, doi:10.1103/PhysRevC.92.045204.

[61] D. H. Wilkinson, Proc. Rutherford Int. Jubilee Conference, Manchester, 1960, Heywood, London.

[62] F. Bossi, et al., Precision Kaon and Hadron Physics with KLOE, Riv. Nuovo Cim. 31 (2008) 531–623. arXiv:0811.1929, doi:10.1393/ncr/i2008-10037-9.

[63] A. Gallo, et al., DAFNE status report, Conf. Proc. C060626 (2006) 604–606.

[64] M. Adinolfi, et al., The tracking detector of the KLOE experiment, Nucl. Instrum. Meth. A488 (2002) 51–73. doi:10.1016/S0168-9002(02)00514-4.

[65] M. Adinolfi, et al., The KLOE electromagnetic calorimeter, Nucl. Instrum. Meth. A482 (2002) 364–386. doi:10.1016/S0168-9002(01)01502-9.

[66] F. Ambrosino, et al., Data handling, reconstruction, and simulation for the KLOE experiment, Nucl. Instrum. Meth. A534 (2004) 403–433. arXiv:physics/0404100, doi:10.1016/j.nima.2004.06.155.

[67] C. Patrignani, et al., Review of Particle Physics, Chin. Phys. C40 (10) (2016) 100001. doi:10.1088/1674-1137/40/10/100001.

[68] K. Piscicchia, $\Lambda(1405)$ measurement through the decay to $\Sigma^0\pi^0$ resulting from K^- meson absorption on ^{4}He and ^{12}C with the KLOE detector, Ph.D. thesis, Università degli Studi di Roma Tre, Rome (2013).

[69] R. Del Grande, K. Piscicchia, S. Wycech, Formation of $\Sigma\pi$ Pairs in Nuclear Captures of K^- Mesons, Acta Phys. Polon. B48 (2017) 1881. arXiv:1711.03427, doi:10.5506/APhysPolB.48.1881.

[70] K. Piscicchia, S. Wycech, C. Curceanu, On the $K^-{}^4\mathrm{He} \to \Lambda\pi^-{}^3\mathrm{He}$ resonant and non-resonant processes, Nucl. Phys. A954 (2016) 75–93. doi:10.1016/j.nuclphysa.2016.05.007.

[71] E. M. Henley, π- meson production by protons on nuclei, Phys. Rev. 85 (1952) 204–215. doi:10.1103/PhysRev.85.204.
URL https://link.aps.org/doi/10.1103/PhysRev.85.204

[72] C. A. Bertulani, Probing nuclear skins and halos with elastic electron scattering, J. Phys. G34 (2007) 315–334. arXiv:nucl-th/0604044, doi:10.1088/0954-3899/34/2/011.

[73] K. Piscicchia, et al., First measurement of the $K^- n \to \Lambda\pi^-$ non-resonant transition amplitude below threshold, Phys. Lett. B782 (2018) 339–345. doi:10.1016/j.physletb.2018.05.025.

[74] F. James, M. Roos, Minuit: A System for Function Minimization and Analysis of the Parameter Errors and Correlations, Comput. Phys. Commun. 10 (1975) 343–367. doi:10.1016/0010-4655(75)90039-9.

[75] F. James, M. Roos, Minuit: Function Minimization and Error Analysis, CERN Program Library Long Writeup D506.

[76] F. James, M. Winkler, MINUIT User's Guide.

[77] E. Oset, H. Toki, A Critical analysis on deeply bound kaonic states in nuclei, Phys. Rev. C74 (2006) 015207. arXiv:nucl-th/0509048, doi:10.1103/PhysRevC.74.015207.

[78] S. Wycech, On Nonmesonic Decays of K Mesonatoms, Acta Phys. Pol. 32 (1967) 161.

[79] T. Sekihara, D. Jido, Y. Kanada-En'yo, Lambda(1405)-induced nonmesonic decay in kaonic nuclei, Phys. Rev. C79 (2009) 062201. arXiv:0904.2822, doi:10.1103/PhysRevC.79.062201.

[80] T. Sekihara, J. Yamagata-Sekihara, D. Jido, Y. Kanada-En'yo, J. Yamagata-Sekihara, D. Jido, Y. Kanada-En'yo, Branching ratios of mesonic and nonmesonic antikaon absorptions in nuclear medium, Phys. Rev. C86 (2012) 065205. arXiv:1204.3978, doi:10.1103/PhysRevC.86.065205.